Triphasic $Ni_2P−Fe_2P−CoP$ heterostructure interfaces for efficient overall water splitting powered by solar energy

Kai Chang [a], Duy Thanh Tran [a,*], Jingqiang Wang [a], Kaixuan Dong [a], Sampath Prabhakaran [a], Do Hwan Kim [b], Nam Hoon Kim [a], Joong Hee Lee [a,c,**]

[a] Department of Nano Convergence Engineering, Jeonbuk National University, Jeonju, Jeonbuk 54896, the Republic of Korea
[b] Division of Science Education, Graduate School of Department of Energy Storage/Conversion Engineering, Jeonbuk National University, Jeonju, Jeonbuk 54896 the Republic of Korea
[c] Carbon Composite Research Center, Department of Polymer-Nano Science and Technology, Jeonbuk National University, Jeonju, Jeonbuk 54896, the Republic of Korea

ARTICLE INFO

ABSTRACT

In this study, we design a triphasic $Ni_2P − Fe_2P − CoP$ heterostructure appearing under the form of a hierarchical 3D core–shell hybrid ($CoP@Ni_2P − Fe_2P$) for bifunctionally catalyzing both hydrogen evolution reaction (HER) and oxygen evolution reaction (OER) in alkaline medium. Density functional theory results indicate that the rich interfaces of $Ni_2P − Fe_2P − CoP$ architecture exhibit the best electronic properties and enhanced multiple electroactive site number with optimum hydrogen adsorption energy, significantly surpassing the CoP, $CoP−Ni_2P$, or $CoP−Fe_2P$ cases. Therefore, the electrolyzer cell of $CoP@Ni_2P − Fe_2P_{(+,−)}$ requires a small operating voltage of 1.51 V to reach 10 mA cm^{-2} during alkaline water splitting, outperforming the commercial catalyst couple of $Pt/C_{(−)}//RuO_{2(+)}$ and numerous earlier reports. In addition, the solar-driven water splitting system demonstrates a high solar-to-hydrogen (STH) conversion of 15.33 %, along with excellent long-term stability. The results open a potential approach to design innovative high-performance electrocatalysts for practical green hydrogen production via electrochemical water splitting process.

1. Introduction

Environmental pollution, global warming, and energy shortages have become critical global issues, and thus searching for renewable and clean energy candidates to replace fossil fuels is emerging as an urgent imperative to reach a future carbon-neutralized society by 2050 [1]. Green hydrogen is rising as a star of clean energy source because of its superior advantages of very high gravimetric energy density and large-scale production possibility without greenhouse gas emission [2]. Besides its use as an efficient energy carrier for fueling vehicles in transportation, hydrogen is also extensively applied for many industrial applications, such as ammonia production, petroleum refining, treating metals, and methanol production. However, approximately 95 % of manufactured hydrogen is currently generated from fossil fuel sources, including natural gas reformation and coal gasification, which annually release about 1 gigaton carbon dioxide into the atmosphere [3]. Recently, solar energy-driven water splitting has been presented as a potential alternative to fossil fuels for sustainable carbon-free hydrogen

generation [4]. In this context, solar energy can be easily collected by solar cell systems, while water electrolysis requires the use of effective catalysts to promote the hydrogen evolution and oxygen evolution reaction at cathode and anode, respectively. Noble metal-based catalysts, including Pt/C and IrO_2 (or RuO_2), have been applied for the water splitting process; however, low reserves, high cost, along with inadequate durability make them difficult to promote for large-scale commercial applications [5]. To lower system costs and facilitate the performance towards water splitting, transition metal-based nanomaterials have been attracting significant research interest for replacing noble metal materials. Among numerous reported non-noble metal-based catalysts, transition metal phosphides (TMPs) have received extensive attention, because of their remarkable catalytic activity, high selectivity, low cost, and versatility [6,7]. In particular, the electronegativity of P atom results in a proton acceptor to reduce the free energy hydrogen adsorption. In addition, the presence of phosphate groups obtained from P oxidation may further effectively avoid the corrosion phenomenon to prolong stability of the catalyst during long-term

---

* Corresponding author.
** Corresponding author at: Department of Nano Convergence Engineering, Jeonbuk National University, Jeonju, Jeonbuk 54896, the Republic of Korea.
E-mail addresses: dttran@jbnu.ac.kr (D.T. Tran), jhl@jbnu.ac.kr (J.H. Lee).

electrolysis operation [8]. In this context, various TMPs-based catalysts with single phase nanostructures, such as Ni-Co-Fe-P nanobricks [9], Co-Ni-P film [10], $Fe_{1-x}Co_xP$ nanosheet arrays [11], and a-CoMoP$_x$ [12],… were reported as potential candidates for water splitting; however, the insufficient active site number with unfavored H adsorption energy and inadequate stability are still critical barriers to prohibit their bifunctional catalytic performances [13]. Interfacial engineering of TMPs-based catalysts has been demonstrated as an effective approach to solve the mentioned issues because the heterostructure interfaces can result in favorable electronic properties with well-adjusted adsorption energy caused by the specific charge redistribution and the improvement of multiple active site number derived from the lattice mismatch, disorders, and more defects [14–18]. Therefore, a list of different biphasic TMPs-based heterostructure catalysts have been developed as efficient bifunctional electrodes for overall water splitting. Wu et al. reported heterogeneous biphasic Ni_2P-Fe_2P microsheet directly synthesized on Ni foam to drive a current density of 10 mA cm^{-2} at a voltage of 1.561 V in 1.0 M KOH [19]. Li et al. constructed a self-supported biphasic Co_xP–Fe_2P heterostructure on Ni foam to allow the overall water splitting at a voltage of 1.61 V to obtain 10 mA cm^{-2} [20]. Meanwhile, Liu et al. developed a bifunctional electrocatalysts based on nanosheets of Cu_3P/Ni_2P heterogeneous interfaces that demands a low voltage of 1.56 V @ 10 mA cm^{-2} [21]. Recently, it is worthy to note that the further interfacing engineering to generate triphasic or multiphasic TMPs-based catalysts with abundant heterointerfaces is a promising strategy to well optimize electronic structure, electroactive surface area, type and number of active sites, thus effectively promoting both HER and OER performances to reach practical-level water splitting application. Regarding this, Cai et al. has revealed the formation of a triphasic Ni_2P–Fe_2P–Ru_2P heterostructure that could excellently enhance the efficiency of overall water splitting with very low voltage along with outstanding stability [22]. Or Xu et al. introduced a bifunctional catalyst of Fe–Co–P multi-heterostructure arrays consisting of CoP, Co_2P and FeP that allows superior overall water splitting performance [23]. Moreover, since such multi-phase phosphide structures are directly grown on high-porosity 3D collectors, the resulting material could well retain large active surface area, due to polymer binder usage being unnecessary, while effectively maximizing the guest–host contact with enhanced conductivity, as well as fast mass diffusion to effectively boost catalyst performances [24,25]. Despite the great merits of triphasic or multiphasic TMPs-based catalysts towards water splitting, the complexity of structure and elemental composition design during the preparation seems a barrier leading to few studies on those systems so far. From a recent study of our group [26], we revealed that the use of Co phosphides to support other active components, such as Ni_2P-MnP, could enhance catalytic activities of the resulting hybrid material. Although exciting achievements have been reported for the developed catalyst, there is room for further improvement of the catalytic performance, reaching practical possibility. Firstly, it is necessary to reduce the size of Co phosphide structures from several micrometers to nano scale for maximizing exposed contact surface to create strong interactions between components, then promoting hetero-charge transfer rate/channels as well as loading more active catalysts per area unit. In addition, a comprehensive investigation of active TMP series from Cr, Mn, Fe, Co, and Ni for HER by Wang et al. via theoretical calculations demonstrated that there are more active sites on Fe, Co, and Ni phosphides along with better spin polarization of projected density of states compared to Mn and Cr phosphides [27]. Therefore, we predict that the interfacing engineering of Ni and Fe phosphides over Co phosphide nanostructures can result in impressively synergistic effects to produce catalytic performances beyond the reported case of Ni and Mn phosphides coupled micro-size Co phosphides.

Inspired by the above findings, triphasic CoP–Ni_2P–Fe_2P heterostructure interfaces under the form of hierarchical 3D core@shell hybrid arrays (CoP@Ni_2P–Fe_2P) attached on porous nickel foam (NF) substrate are rationally designed for the first time. The effective interface engineering with optimum adjustment of composition and structure results in the CoP@Ni_2P–Fe_2P hybrid having unique electronic interactions, more active sites, high electronic conductivity, and optimized hydrogen adsorption free energy (ΔG_{H*}), thus exhibiting superior electrocatalytic activities toward both HER and OER in alkaline medium. The developed two-electrode electrolyzer requires a low operating voltage, while the solar driven water splitting process achieves a high STH conversion efficiency of 15.33%, superior to those of commercial catalyst systems, as well as early literature reports.

2. Experimental section

2.1. Materials

Cobalt(II) nitrate hexahydrate (Co(NO$_3$)$_2$·6 H$_2$O, $\geq$ 98.0 %), ammonium fluoride (NH$_4$F, $\geq$ 98.0 %), urea (CO(NH$_2$)$_2$, $\geq$ 99.5 %), nickel (II) nitrate hexahydrate (Ni(NO$_3$)$_2$·6 H$_2$O, 99.9 %), iron(II) sulfate heptahydrate (FeSO$_4$·7 H$_2$O, $\geq$ 99.0 %), sodium hypophosphite monohydrate (NaH$_2$PO$_2$·H$_2$O, 99.9 %), nafion solution (5 wt%), platinum on graphitized carbon (Pt/C, 20 wt%), and ruthenium (IV) oxide (RuO$_2$, 99.9 %) were purchased from Sigma–Aldrich Chemicals Co., Ltd. (USA). Ethanol (C$_2$H$_5$OH, 99 %), hydrochloric acid (HCl, 37.5 wt%), and potassium hydroxide pellets (KOH, 85 %) were provided by Samchun Co., Ltd. (Korea).

2.2. Fabrication of CoP NWs on NF

In a specific procedure, 5 mmol of Co(NO$_3$)$_2$·6 H$_2$O, 10 mmol of NH$_4$F, and 25 mmol of CO(NH$_2$)$_2$ were dissolved in 75 mL of deionized (DI) water, followed by magnetic stirring to form a well-dispersed solution. The solution was then added into a Teflon autoclave containing a clean NF substrate (3 cm × 4 cm), to conduct a hydrothermal reaction at 120 °C for 5 h. When the reaction was completed, the system was naturally cooled, and the sample was collected for a subsequent washing step and drying at 60 °C for overnight. The synthesized sample (located downstream) and 1 g of NaH$_2$PO$_2$·H$_2$O were then placed in quartz boat inside a tube furnace to undergo a phosphidization process at 350 °C for 1 h under an argon flow rate of 100 sccm with a heating rate of 3 °C min^{-1}.

2.3. Fabrication of CoP@Ni$_2$P–Fe$_2$P on NF

Initially, cobalt phosphide nanowire arrays (CoP NWs) on NF (1 cm × 2 cm) were used as working electrodes to grow NiFe hydroxide nanosheets (NSs) via an electrodeposition step for 50 s at − 1.0 V in a solution consisting of 100 mL DI water, 15 mmol Ni(NO$_3$)$_2$·6 H$_2$O, and 15 mmol FeSO$_4$·7 H$_2$O. The sample was then washed by DI water and dried at 60 °C, to obtain CoP@NiFe hydroxide arrays on NF. After that, the CoP@NiFe hydroxide arrays on NF and 0.6 g NaH$_2$PO$_2$·H$_2$O were put at downstream and upstream locations in a quartz boat, respectively, to undergo a phosphidization process at 350 °C in argon atmosphere at a flow rate of 100 sccm for 1 h to produce CoP@Ni$_2$P – Fe$_2$P catalyst, which has a loading of about 8.9 mg on 1.0 cm^{-2} of NF.

2.4. Materials characterizations

The morphology and structure of the synthesized materials were characterized by field-emission scanning electron microscopy (FE−SEM), and energy dispersive spectroscopy (EDS) on a Supra 40 VP instrument (Zeiss, Germany). The microstructures were analyzed using transmission electron microscopy (TEM) and high-resolution TEM (HR−TEM) with an operating voltage of 120 kV. They were studied on JEM−ARM200F instrument (JEOL Co., USA) at the Jeonju Center of the Korea Basic Science Institute. To determine the phase composition of the materials, X-ray diffraction (XRD) tests were carried out with Cu−Kα radiation (λ = 0.154 nm) from (10−80)° through a Rigaku D/max 2400

X-ray generator at the Center for University-wide Research Facilities, Jeonbuk National University, Korea. The elemental composition and chemical state of the materials were evaluated using X-ray photoelectron spectroscopy (XPS) on a Theta Probe instrument (Thermo Fisher Scientific, Inc., USA). The specific surface area of the materials was checked by Brunauer–Emmett–Teller and Barrett–Joyner–Halenda models (ASAP 2020 Plus system, Micromeritics Instrument Corp., USA). The active substances before and after the electrochemical reaction were analyzed by Raman spectrum using a Nanofinder-30 instrument from Tokyo Instruments, Japan.

2.5. Electrochemical characterizations

The performance of the materials was evaluated at room temperature using a CHI660D (CH Instruments Inc. USA) electrochemical workstation. Linear-sweep voltammetry (LSV) curves of HER and OER were measured by a three-electrode system in 1.0 M KOH aqueous solution at a sweep rate of 2 mV s^{-1}, and then corrected by iR-compensation (100 %), where synthesized materials (1 cm × 1 cm) were used as the working electrode, graphite rod as the counter electrode, and Ag/AgCl as the reference electrode. The current difference of the cyclic voltammetry (CV) curves at 0.98 V (vs. RHE) was linearly fitted at different scanning speeds of (20, 40, 60, 80, and 100) mV s^{-1}. Half of the linear slope is the double-layer capacitances (C_{dl}) of the materials, which is proportional to

the electrochemical surface area (ECSA). The materials were analyzed by electrochemical impedance spectroscopy (EIS) to assess charge transfer resistance (R_{ct}) at the interfacial area between the electrode and electrolyte with scanning frequencies of from (10^5 to 10^{-2}) Hz. The stability of catalysts was characterized through changes in LSV before and after 2000 CV cycles and chronoamperometry. The potentials obtained from the experiments were converted into reversible hydrogen electrode (RHE) [28]:

$$E \ (V \ vs \cdot RHE) = E_{Ag/AgCl} + 0 \cdot 197 + 0 \cdot 0591 \times pH \tag{1}$$

The performance of the devices based on CoP@Ni$_2$P $-$ Fe$_2$P$_{(+,-)}$ and Pt/C$_{(-)}$//RuO$_{2(+)}$ were evaluated by LSV in alkaline water at a sweep rate of 1 mV s^{-1}, respectively. To calculate the Faraday efficiency of the catalysts, the volumes of hydrogen and oxygen produced during the electrocatalytic reaction were collected using the drainage method. The corresponding theoretical hydrogen and oxygen volumes were then determined by assuming that 100 % of the current output of the working electrode was used to carry out the catalytic reaction. In the solar driven water splitting part, the entire system consists of a commercial solar cell (5 cm × 5 cm, effective surface area: 11.55 cm^2) and electrolyzer, in which a HAL-320 solar simulator (Asahi Spectra Co., Ltd., Japan) was used to generate AM 1.5 G illumination to maximize the simulation of sunlight. The following equation was used to calculate the efficiency of STH [29]:
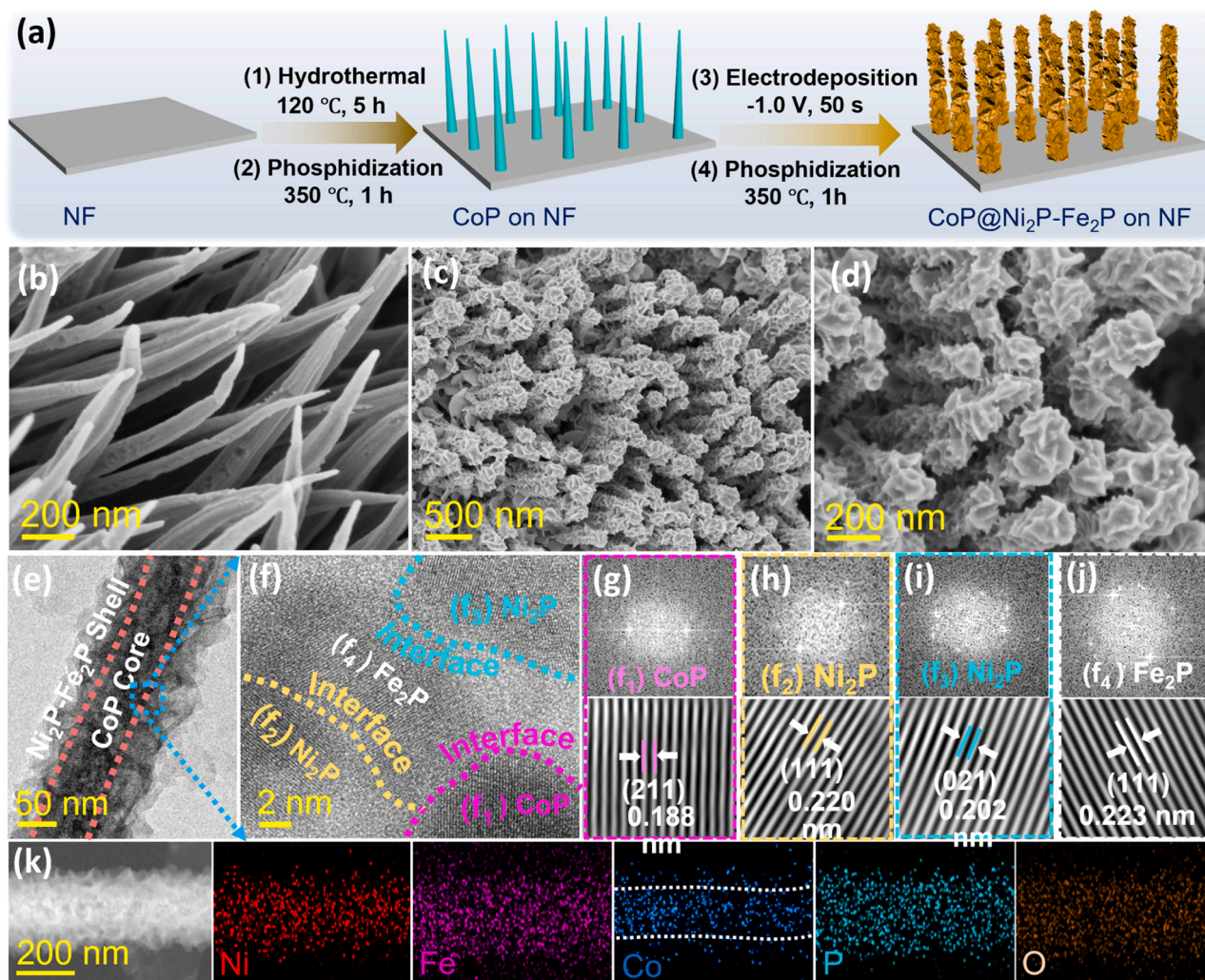

Fig. 1. (a) Schematic of the preparation of CoP@Ni$_2$P $-$ Fe$_2$P on NF; FE−SEM images of (b) CoP, and (c) & (d) CoP@Ni$_2$P $-$ Fe$_2$P on NF; (e) TEM images of a CoP@Ni$_2$P $-$ Fe$_2$P structure; (f) HR−TEM image at an interfacial area of CoP−Ni$_2$P $-$ Fe$_2$P; (g)–(j) FFT and IFFT patterns of different phases; (k) STEM image of CoP@Ni$_2$P $-$ Fe$_2$P along with EDS color mapping images for Ni, Fe, Co, P, and O elements.

$$STH\% = (J \times 1 \cdot 23 \text{ V})/100 \text{ mW cm}^{-2} \qquad (2)$$

For comparison, we evaluated the activities of RuO_2 and 20 wt% Pt/C. In detail, 8.9 mg Pt/C (or RuO_2) powder was dispersed in a mixed solution consisting of 50 μL Nafion, 750 μL isopropanol, and 200 μL DI water to form a homogeneous ink by sonication. The ink was then uniformly dropped on the surface of NF (1 cm × 1 cm) and dried at 60 °C overnight.

3. Results and discussion

3.1. Structural characterizations

Fig. 1a shows the fabrication process of the triphasic CoP−Ni_2P − Fe_2P heterostructure interfaces under the form of 3D hierarchical core–shell hybrid arrays. In this context, vertical one-dimensional (1D) CoP NWs of uniform size and high density are initially prepared on NF substrates by a simple hydrothermal reaction and subsequent phosphidization step (Fig. S1a and Fig. 1b). The NWs have a length of about several micrometers, along with good crystalline behavior that is suitable for the specific features of a CoP structure (PDF#29-0497) (Figs. S1b–e) [30]. The well-crystallized CoP NWs provide high mechanical properties and a large specific surface area that is highly beneficial for a subsequent coating step of Ni_2P − Fe_2P heterostructure having rich exposed active sites and excellent interfacial hetero-charge transfer ability [31]. After suffering a rapid electrodeposition step to form two-dimensional (2D) bimetallic Ni-Fe hydroxide based NSs uniformly coating CoP NWs (Fig. S2) [32], a second phosphidization treatment is applied for the achieved hydroxide material to produce the CoP@Ni_2P − Fe_2P heterostructure hybrid. Fig. 1c and d show that abundant crinkled and twisted NSs fully coat over 1D CoP structure to form a unique heterostructure with highly porous characteristic. The same micromorphology is also observed for the synthesized samples of CoP@Ni_2P and CoP@Fe_2P materials (Fig. S3). The TEM image in Fig. 1e further indicates that those NSs are interconnected together to form a gray−colored layer having a thickness of about (40 −50) nm covering an entire dark−colored CoP structure. The HR−TEM image of Fig. 1f clearly presents the formation of a multiphase heterostructure with CoP, Ni_2P, and Fe_2P having well-defined boundaries.

Fig. 1g–j show the high-angle annular dark-field (HAADF)−STEM images and fast Fourier transform (FFT) spectra collected from different areas of f_1–f_4 in Fig. 1f, which reveal specific lattice fringes with interspacing of (0.188, 0.220, 0.202 and 0.223) nm, well matching the CoP (211), Ni_2P (111), Ni_2P (021), and Fe_2P (111) crystal planes, respectively, implying the nature of a triphasic CoP−Ni_2P − Fe_2P heterostructure [33–35]. The STEM−EDS color mapping images in Fig. 1k show the presence of Ni, Fe, Co, P, and O elements in the hybrid material, in which the intensity of Co signal is concentrated at the inner core part, while the Ni, Fe, P, and O signals are homogeneously spread over the entire structure, interestingly confirming the formation of the core@shell CoP@Ni_2P − Fe_2P architecture. Such achieved heterostructure hybrid results in a direct contact between CoP−Ni_2P − Fe_2P phases and between those with NF substrate with good interaction, thus expecting to ensure an efficient hetero-charge transfer and strong mechanical structure. In addition, the bimetallic phosphide NSs of Ni_2P − Fe_2P with high porosity and extensive edges could endow more in-plane defects and multiple electroactive sites to improve the catalyst performances [36].

The crystalline heterostructure interfaces of the CoP@Ni_2P − Fe_2P were further studied by XRD analysis. Fig. 2a shows that along with the strong intensities of signals coming from Ni metal substrate, its XRD pattern also displays specific diffraction peaks corresponding to the crystalline features of the CoP phase (JCPDF#29−0497), Ni_2P phase (JCPDF#65−9706), and Fe_2P phase (JCPDF#88−1803), which are well consistent with the TEM results [37–39], thus further demonstrating the formation of the CoP−Ni_2P − Fe_2P heterostructure. The interaction between the Ni_2P, Fe_2P, or Ni_2P − Fe_2P shell layer with CoP caused by their different electronegativity and crystalline mismatch is identified by the high-magnification XRD patterns in the 2θ range from 35.7° to 37° (Fig. 2b). The achieved interfaces show a down shifting of the CoP (111) peaks, as compared to that of the pure CoP material. In particular, a more negative shifting is observed for the case of the Ni_2P − Fe_2P shell,
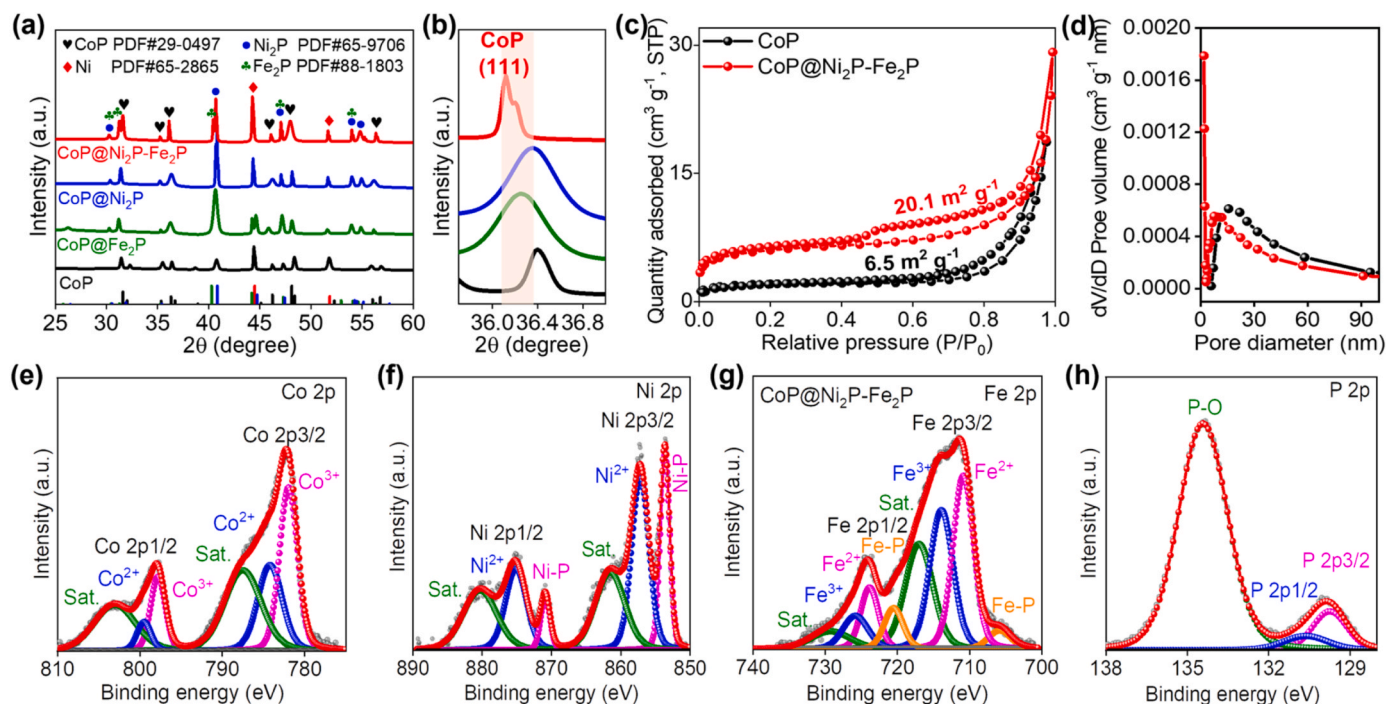

Fig. 2. (a) XRD patterns of the different synthesized catalysts, and (b) their high-magnification XRD patterns in the 2θ range (35.7 − 37)°; (c) Nitrogen adsorption–desorption isotherms of the CoP and CoP@Ni_2P − Fe_2P materials, and (d) their porous distribution; HR−XPS spectra of the (e) Co 2p, (f) Ni 2p, (g) Fe 2p, and (h) P 2p binding energies from CoP@Ni_2P − Fe_2P.

as compared to the Ni_2P or Fe_2P shell, clearly identifying that a combined $Ni_2P - Fe_2P$ heterostructure is helpful toward increasing the lattice deformation of CoP, Ni_2P, and Fe_2P shell. Such a phenomenon creates more atomic defects as electroactive sites to be useful for boosting the catalytic performance of the electrocatalyst [40,41]. In another regard, the formation of $CoP@Ni_2P - Fe_2P$ heterogeneous structure shows unique micropore features with an enlarged specific surface area that is about 3.1 times higher (Fig. 2c) and superior pore volume (Fig. 2d), as compared to the pure CoP material, thus expecting to create more exposed active sites for improved catalytic activities [42]. The surface chemistry along with electronic modifications due to the different electronegativity of crystalline phases and their interactions in the heterostructure hybrid is studied by XPS analysis. Initially, the survey XPS spectrum of $CoP@Ni_2P - Fe_2P$ indicates its composition of Co, Ni, Fe, P, and O elements (Fig. S4). In addition, the high-resolution XPS (HR-XPS) spectrum of the Co 2p binding energy in Fig. 2e shows the presence of three peak doublets assigned to Co^{3+} (781.7 and 797.9) eV, Co^{2+} at (783.7 and 799.8) eV, and corresponding satellite species at (787.2 and 803.2) eV. Moreover, the peaks located at 778.4 and 793.5 eV can be attributed to the Co-P bonds [43]. The HR-XPS spectrum of Ni 2p binding energy could also be deconvoluted into three peak doublets associated with $Ni^{\delta+}$ in the Ni-P bonds ($0 < \delta < 2$) at (853.1 and 870.1) eV, Ni^{2+} at (856.9 and 874.8) eV, and satellite species at

(861.5 and 880.3) eV (Fig. 2f) [13]. The HR-XPS spectrum of Fe 2p binding energy of Fig. 2g is fitted with four peak doublets located at ((705.9 and 720.6), (710.9 and 723.9), (713.8 and 725.8), and (717.2 and 729.3)) eV, consistent with Fe-P bonding, Fe^{2+}, Fe^{3+}, and satellite portion, respectively [44,45]. The HR-XPS spectrum of P 2p binding energy shows two specific behaviors (Fig. 2h), in which the signals at (129.6 and 130.5) eV are attributable to P $2p3/2$ and P $2p1/2$, respectively, derived from the characteristics of P-metal bonding (Co-P, Ni-P, or Fe-P) in the metal phosphide structures, while a peak at 134.1 eV results from P - O bonding in the metal phosphate portions caused by surface oxidation during the synthetic process or storage in air environment [46].

Impressively, since the HR-XPS spectra of Co 2p and P 2p binding energies from the $CoP@Ni_2P - Fe_2P$, $CoP@Ni_2P$, and $CoP@Fe_2P$ are shifted to higher value as compared to those from CoP. In addition, it could be also revealed a certain negative shifting of Ni 2p or Fe 2p binding energy from $CoP@Ni_2P - Fe_2P$ as compared to those of $CoP@Ni_2P$ or $CoP@Fe_2P$ material, suggesting a charge redistribution phenomenon around metal centers due to the good interaction between $CoP-Ni_2P-Fe_2P$ (Fig. S5), thereby producing modified valence states of metal centers to improve the catalytic performances [47–49].
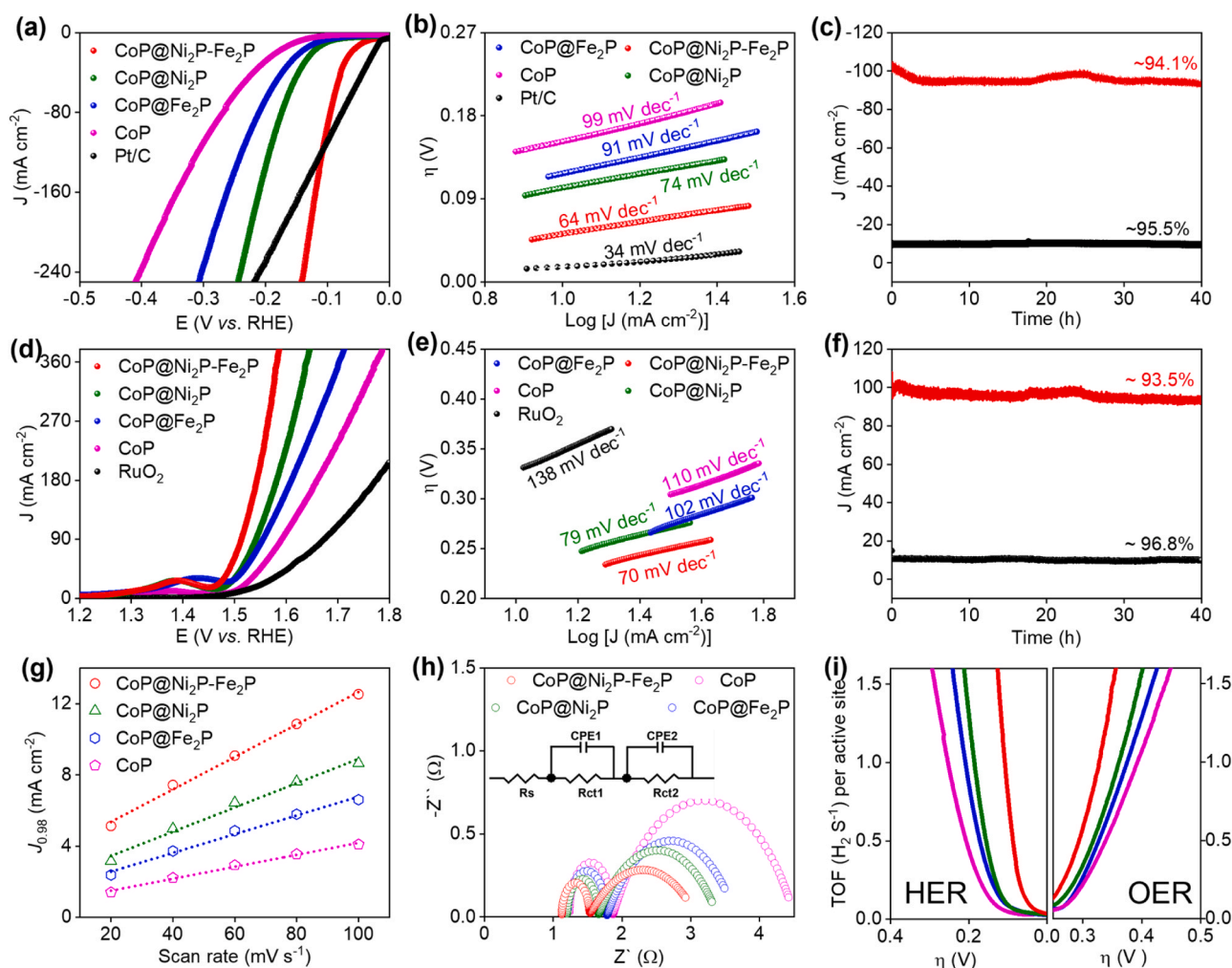

Fig. 3. (a) iR-corrected LSV curves, and (b) Tafel slopes, of the different as-prepared catalysts for alkaline HER process; (c) Chronoamperometric response of the $CoP@Ni_2P - Fe_2P$ catalyst operating at initial current densities of (10 and 100) mA cm^{-2} toward alkaline HER; (d) iR-corrected LSV curves, and (e) Tafel slopes, of the different as-prepared catalysts for alkaline OER process; (f) Chronoamperometric response of the $CoP@Ni_2P - Fe_2P$ operating at initial current densities of (10 and 100) mA cm^{-2} for alkaline OER; (g) C_{dl} plots of different synthesized catalysts; (h) Nyquist plots of different synthesized catalysts in a frequency range from 10^5 to 10^{-2} Hz in alkaline water; (i) Calculated H_2 and O_2 TOF values of CoP, $CoP@Fe_2P$, $CoP@Ni_2P$, and $CoP@Ni_2P-Fe_2P$.

3.2. Catalytic performances

The electrocatalytic performances of the prepared catalysts towards HER and OER were initially studied in alkaline medium (1.0 M KOH) at a sweep rate of 2 mV s^{-1}. Fig. 3a shows the iR-corrected LSV curves of the HER process, which indicates the superior current response and overpotential (η) of the CoP@Ni$_2$P − Fe$_2$P, as compared to the other catalysts. Specifically, the CoP@Ni$_2$P − Fe$_2$P only requires an η value of 42/101 mV at current output of 10/100 mA cm^{-2}, respectively, much smaller than that of CoP@Ni$_2$P (103/185 mV), CoP@Fe$_2$P (117/ 225 mV), or CoP (152/290 mV) (Fig. S6). Such achievement also surpasses the results of many recently reported studies (Table S1). In particular, the catalytic behaviors of CoP@Ni$_2$P − Fe$_2$P are also superior to those of the commercial Pt/C at its current response higher than 110 mA cm^{-2}. The HER reaction kinetics of the catalysts are evaluated by using Tafel slopes derived from their consistent LSV curves. The Tafel slope of the CoP@Ni$_2$P − Fe$_2$P is found to be 64 mV dec^{-1}, considerably lower than that of the CoP@Ni$_2$P (74 mV dec^{-1}), CoP@Fe$_2$P (91 mV dec^{-1}), and CoP (99 mV dec^{-1}), respectively (Fig. 3b). This observation suggests that the HER process occurs on the surface of CoP@Ni$_2$P − Fe$_2$P catalyst via the Volmer–Heyrovsky mechanism, in which the Heyrovsky step determines the reaction rate [50]. Stability is an important criterion for evaluating the practicability of an electrocatalyst. Excitingly, the CoP@Ni$_2$P − Fe$_2$P exhibits a prospective overlapping of current response with minor increase of η after 2000 cycles of continuous CV test (Fig. S7). In addition, the current–time responses of CoP@Ni$_2$P − Fe$_2$P measured by chronoamperometry at initial current responses of 10 and 100 mA cm^{-2} in Fig. 3c indicate the good retention of 95.5 % and 94.1 %, respectively, after suffering 40 h of testing, further evidencing the excellent stability of the CoP@Ni$_2$P − Fe$_2$P for HER in alkaline medium. The morphology and structure of the post-HER CoP@Ni$_2$P − Fe$_2$P sample were also investigated by SEM and TEM analyses (Fig. S8). Its micromorphology is well preserved with uniform 1D hierarchical CoP@Ni$_2$P − Fe$_2$P NWs densely attached on the NF surface. The structure of the shell layer recognizes the specific interspacing of (0.223 and 0.220) nm consistent with the (111) crystal planes of the Fe$_2$P and Ni$_2$P phases, respectively.

The OER performance of the synthesized catalysts and the commercial RuO$_2$ were also evaluated at a sweep rate of 2 mV s^{-1} in 1.0 M KOH medium. The iR-corrected LSV curves show anodic peaks at around 1.4 V, suggesting an oxidative transformation of metal on the surface of catalysts before the OER process starts (Fig. 3d). In addition, the LSV results also indicate that the CoP@Ni$_2$P − Fe$_2$P needs an η value as low as 287/319 mV to attain current output of 100/200 mA cm^{-2}, out-performing that of the CoP@Ni$_2$P (316/359 mV), CoP@Fe$_2$P (331/ 391 mV), CoP (369/444), and commercial RuO$_2$ (456/563 mV) (Fig. S9). Such η value of CoP@Ni$_2$P − Fe$_2$P is also one of the emerging research results obtained from the transition metal-based electro-catalysts as reported so far (Table S2). The Tafel plots in Fig. 3e show a small Tafel slope value of 70 mV dec^{-1} for the CoP@Ni$_2$P − Fe$_2$P, which is significantly lower than that of the CoP@Ni$_2$P, CoP@Fe$_2$P, CoP, and commercial RuO$_2$ with 79, 102, 110, and 138 mV dec^{-1}, respectively, demonstrating the superior OER kinetics of the CoP@Ni$_2$P − Fe$_2$P among the prepared catalysts in alkaline medium. We also assess the OER stability of CoP@Ni$_2$P − Fe$_2$P catalyst by CV test. Fig. S10 shows only a minor decrease of current response and η after 2000 CV cycles. The chronoamperometric measurement for CoP@Ni$_2$P − Fe$_2$P electrode at the initial current response of (10 and 100) mA cm^{-2} also indicates a current loss of (6.5 and 3.2) %, respectively, after 40 h OER operation (Fig. 3 f). These results further confirm the good stability of the CoP@Ni$_2$P − Fe$_2$P catalyst for long-term OER process in alkaline medium. The excellent OER performance of the TMPs electrocatalysts is usually consistent with a surface modulation with an in-situ formation of metal oxide/(oxy)hydroxide species since they work at an applied anodic potential [51,52]. Therefore, the morphology, structure, and elemental valence states of the post-OER CoP@Ni$_2$P − Fe$_2$P sample were

investigated. Although the FE-SEM (Figs. S11a–c) and TEM images (Figs. S11d and e) indicate the sample still retains its pristine micro-morphological behavior with hierarchical 3D architecture of core@shell heterostructure arrays uniformly loading on NF substrate. The insight into the structure observed by HR−TEM analysis shows that the shell layer of Ni$_2$P − Fe$_2$P suffers an oxidization phenomenon during the OER process. Specifically, it can be seen the lattice spacing of 0.239 and 0.260 nm, corresponding to the (011) plane of Ni(OOH) and the (110) plane of Fe(OOH), respectively (Figs. S11f–i) [53]. Raman analysis also interestingly confirms the TEM result with a consistent spectrum in Fig. S12, which exhibits that while the pristine material has no Raman response, the post-OER sample clearly shows two specific Raman bands at (481.2 and 554.9) cm^{-1} of the Ni(OOH) part, as well as a band at 675.1 cm^{-1} that was attributed to the Fe–O vibrations of the Fe(OOH) part [54]. The TEM and Raman observations are further supported by the surface chemistry characteristics of the post-OER sample via XPS analysis. In this context, Fig. S13a recognizes an increase of the O element content, whereas the P content is decreased. In addition, the HR−XPS spectra of the Co 2p, Ni 2p, Fe 2p, P 2p, and O 1 s binding energies from the post-OER sample exhibit significant changes of shape, intensity, and peak position, as compared to those of the pristine one. It can be seen in Figs. S13b and c, the HR-XPS Co 2p and Ni 2p spectrum shows the disappearance of the Co-P and Ni−P peak, respectively, together with the emergence of Ni^{3+} peaks at (857.4 and 875.1) eV. The HR−XPS Fe 2p spectrum reveals the disappearance of the Fe–P peak, along with an increase of the high- valency Fe^{3+}/Fe^{2+} intensity ratio (Fig. S13d). The weak P 2p spectrum of the post-OER sample also recognizes a strong peak of phosphate component, while the phosphide portion is almost invisible (Fig. S13e). Furthermore, the HR−XPS O 1 s spectrum also displays the rise of a specific peak relating to M−O bond (Fig. S13f). The above XPS results demonstrate an in situ oxidation process occurring on surface of the catalyst during anodic scan to generate higher valence states of Ni and Fe under the form of oxide or (hydroxyl) oxide layer, known as the active sites to promote OER process (Fig. S14) [55]. Meanwhile, the phosphates also own the capability to exhibit as a labile ligand, which could alter its coordination or chelating modes during the redox switching procedure of the metal ion and assist to promote the OER [56].

To understand the enhanced catalytic HER and OER performances of the CoP@Ni$_2$P − Fe$_2$P, the ECSA and charge transfer ability of the synthesized catalysts were studied. As an important indicator of active site number, the ECSA value of the catalysts is evaluated by measuring the C$_{dl}$, which is obtained from the CV response at different sweep rates in a non-Faraday potential region. From the CV results of the catalysts at a scan rate of 20, 40, 60, 80, and 100 mV s^{-1} in Fig. S15, it is found that CoP@Ni$_2$P − Fe$_2$P possesses the largest CV area among all survey catalysts at a scan rate of 20 mV s^{-1} (Fig. S16). Moreover, Fig. 3 g indicates that it also has a high C$_{dl}$ value of 41.39 mF cm^{-2}, significantly better than that of CoP@Ni$_2$P, CoP@Fe$_2$P, and CoP with 34.12, 26.34, and 16.82 mF cm^{-2}, respectively. This allows the CoP@Ni$_2$P − Fe$_2$P to generate more active sites to participate in the catalytic reactions [57]. The advanced reaction kinetics of CoP@Ni$_2$P − Fe$_2$P are also elucidated by the Nyquist plot achieved from the EIS measurement. Fig. 3 h exhibits the smallest semicircle part for CoP@Ni$_2$P − Fe$_2$P as compared to the other catalysts, implying its superior charge transfer ability at the interface to promote the reactions. We also estimated the ability of each active site to perform electrochemical reactions, known as turnover frequency (TOF(η), s^{-1}), for further identifying intrinsic activity of the catalysts [58]. By measuring the number of active sites via CV method at a sweep rate of 50 mV s^{-1} in PBS solution (Fig. S17) [59], the HER and OER TOF values of the catalysts are calculated and then shown in Fig. 3i. The highest TOF values of CoP@Ni$_2$P − Fe$_2$P over the survey potential region further confirm its superior intrinsic catalytic activity towards HER and OER in alkaline medium [60].

The advantages of the triphasic heterogeneous interfaces derived from CoP−Ni$_2$P − Fe$_2$P were also identified by using theoretical density

functional theory (DFT) study for the calculation of density of states (DOS) and ΔG_{H*} using the VASP computational package. Fig. 4a shows the different structural models, including CoP, CoP@Ni$_2$P, CoP@Fe$_2$P, and CoP@Ni$_2$P – Fe$_2$P, applied for the DFT study. From the electrocatalysis perspective, a catalyst having high DOS value at near Femi level and an optimized ΔG_{H*} closer to 0 eV is advantageous for promoting catalytic performance [61]. In this context, Fig. 4b shows that the CoP@Ni$_2$P – Fe$_2$P has an excellent DOS result, superior to CoP, CoP@Ni$_2$P, and CoP@Fe$_2$P at near Femi level, suggesting its favorite electronic structure with improved conductivity [62]. Fig. 4c shows the ΔG_{H*} values of different developed catalysts, including CoP, CoP@Ni$_2$P, CoP@Fe$_2$P, and CoP@Ni$_2$P – Fe$_2$P. It could be seen that the ΔG_{H*} value of CoP@Ni$_2$P – Fe$_2$P is calculated to be − 0.091 eV, which is closer to 0 eV than that of CoP@Ni$_2$P, CoP@Fe$_2$P, and CoP with − 0.097, − 0.099, and 0.172 eV, respectively, indicating that the CoP@Ni$_2$P – Fe$_2$P structure can effectively reduce the surface reaction kinetic energy barrier for HER process. Moreover, the formation of the multi-interfacial CoP@Ni$_2$P – Fe$_2$P structure also leads to the explosion of various types of atomic sites exposed on the surface, which can display an important contribution for accelerating the intrinsic catalytic

activity. To clarify the main active site of CoP@Ni$_2$P – Fe$_2$P heterostructure, the DFT calculation of ΔG_{H*} was carried out for different atomic sites on its surface, including Co in CoP phase (site 1), P in CoP phase (site 2), Ni in Ni$_2$P phase (site 3), P in Ni$_2$P phase (site 4), Fe in Fe$_2$P phase (site 5), and P in Fe$_2$P phase (site 6) (Fig. 4d). The results show that the site 3 of Ni atom in Ni$_2$P phase (3) has a ΔG_{H*} value of − 0.091 eV, which is better than that of site 1, site 2, site 4, site 5, and site 6 with their ΔG_{H*} values of − 0.115, − 0.213, − 0.093, − 0.467, and − 0.491 eV, respectively, demonstrating that such Ni centers are the primary active sites for catalyzing the HER process (Fig. 4e). This achievement may result from the fact that the formation of multi-interfacial CoP@Ni$_2$P – Fe$_2$P structure creates a unique charge redistribution with electron transfer to Ni$_2$P phase to form an optimized electronic structure of Ni site and motivate its ΔG_{H*} to a closer-to-zero value, thereby obtaining superior HER catalytic behavior as compared to other sites [63]. To understand the effect of interface formation on the electrocatalytic activities of CoP@Ni$_2$P – Fe$_2$P, we calculated ΔG_H* values of atomic sites at interface of Ni$_2$P – Fe$_2$P hetero-phase to compare with those on its surface. Fig. S18 and Table S3 shows that ΔG_H* values of the sites on surface of Ni$_2$P – Fe$_2$P hetero-phase are
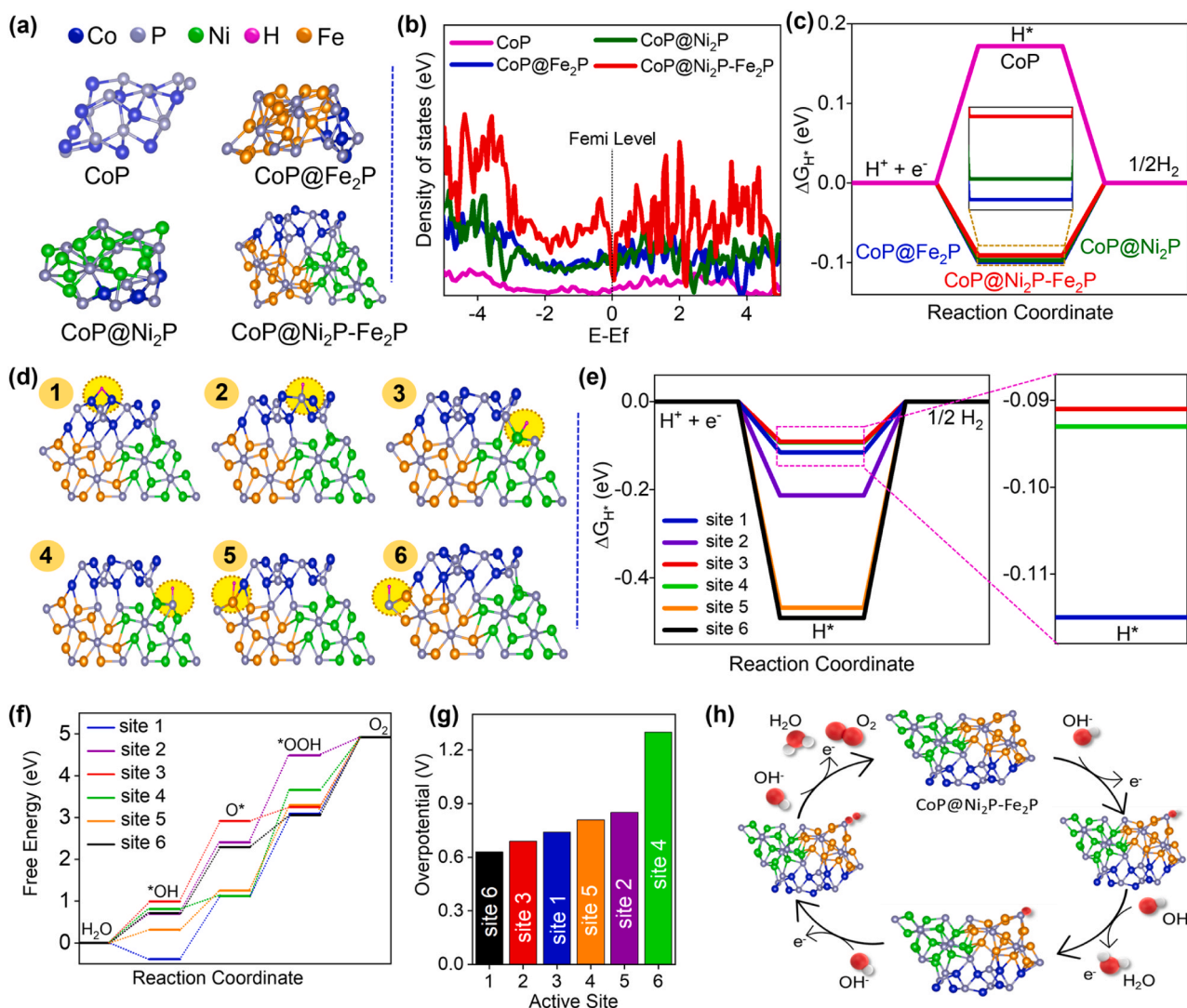

Fig. 4. (a) The theoretical structure models of different developed catalysts, including CoP, CoP@Fe$_2$P, CoP@Ni$_2$P, and CoP@Ni$_2$P – Fe$_2$P for DFT calculation; (b) DOS values of different theoretical catalyst models; (c) ΔG_{H*} values of different catalyst models; (d) H adsorption at different active centers on surface of CoP@-Ni$_2$P – Fe$_2$P catalyst; (e) ΔG_{H*} values of different active centers from the CoP@Ni$_2$P – Fe$_2$P catalyst; (f) Free energy diagram of different active centers on surface of CoP@Ni$_2$P – Fe$_2$P catalyst towards a four-step OER process; (g) Overpotential values of different centers from CoP@Ni$_2$P – Fe$_2$P catalyst towards a four-step OER process; (h) Schematic illustration of the OER mechanism occurring at site 6 (P atomic center of Fe$_2$P) of CoP@Ni$_2$P – Fe$_2$P catalyst.

better than those at the interface region. This result suggests that the formation of CoP@Ni$_2$P – Fe$_2$P interfaces efficiently modulates electronic properties of atomic sites on the surface to obtain an optimum free energy for H adsorption. In addition, the mismatch lattice at interfaces

results in numerous disorders and defects to offer rich catalytically active centers [26,64]. Moreover, the achieved multiple interfaces not only generate more channels and excellent catalyst−electrolyte contact for accelerating mass and charge transport but also lead to the robust
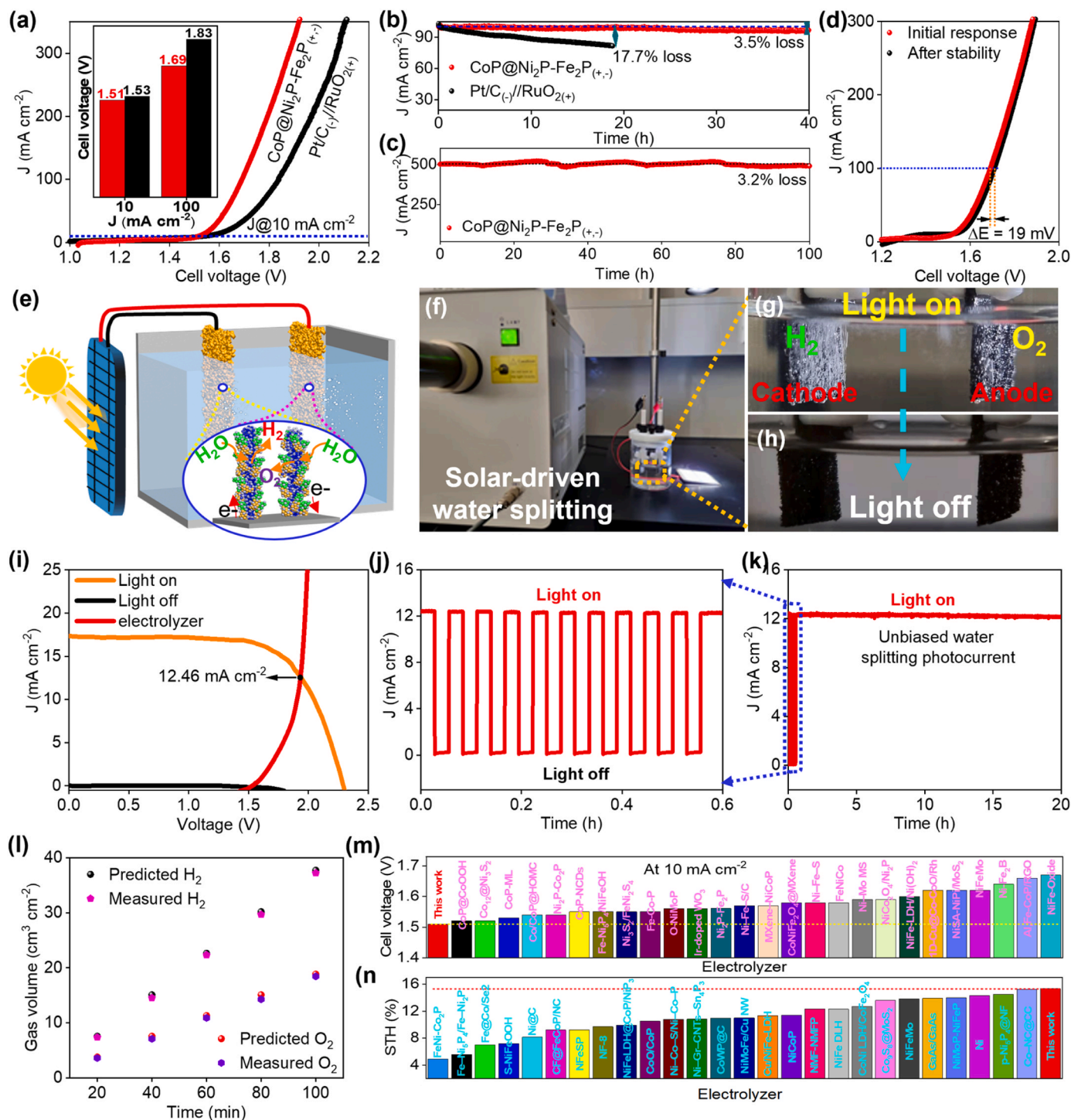

Fig. 5. (a) iR-corrected LSV curves of CoP@Ni$_2$P – Fe$_2$P$_{(+,-)}$ and Pt/C$_{(-)}$//RuO$_{2(+)}$ cells for overall alkaline water splitting (Inset: Cell voltages of CoP@Ni$_2$P – Fe$_2$P$_{(+,-)}$ and Pt/C$_{(-)}$//RuO$_{2(+)}$ at (10 and 100) mA cm^{-2}); (b) Chronoamperometric stability of CoP@Ni$_2$P – Fe$_2$P$_{(+,-)}$ and Pt/C$_{(-)}$//RuO$_{2(+)}$ cells at 100 mA cm^{-2} during 40 h operation in alkaline medium; (c) Chronoamperometric stability of CoP@Ni$_2$P – Fe$_2$P$_{(+,-)}$ at 500 mA cm^{-2} during 100 h operation in alkaline medium; (d) LSV curves of the CoP@Ni$_2$P – Fe$_2$P$_{(+,-)}$ before, and after, stability test; (e) Schematic of a solar driven water splitting system; (f)–(h) Optical images of the solar driven water splitting system and its operation under light-on and light-off condition; (i) J−V curve of a solar cell under simulated AM 1.5 G illumination and LSV curve of CoP@Ni$_2$P – Fe$_2$P$_{(+,-)}$ cell toward alkaline water splitting; (j and k) J–t curve of the integrated alkaline water splitting device under chopped simulated AM 1.5 G illumination; (l) Faradaic efficiency of the CoP@Ni$_2$P-Fe$_2$P$_{(+,-)}$ electrolyzer towards water splitting in alkaline medium; Comparison of (m) cell voltage, and (n) STH efficiency, between the CoP@Ni$_2$P – Fe$_2$P$_{(+,-)}$ cell and previous studies.

interactions among material phases to produce superior electronic conductivity and great mechanical stability for improving catalytic performances [65].

The DFT calculation of OER mechanism for a four-step OER process with free energy of each primary reaction step was also studied for the CoP@Ni$_2$P – Fe$_2$P catalyst. Fig. 4 f indicates the OER process occurring at different atomic sites on surface of the catalyst, in which the transition of *OH to O* and *OOH to O$_2$ is the rate-controlling step of the site 3 and site 6, respectively, while the formation of O* from *OOH is the rate-controlling step of site 1, site 2, site 4, and site 5. A better free energy change of the rate-determining step for site 6 suggests its smaller energy barrier in the generation of adsorbed intermediates as compared to other sites (Table S4), thus resulting in fast O$_2$ kinetic. In addition, it is worth noting that site 6 has the smallest theoretical η value of 0.63 V among all exposed atomic sites on surface of the catalyst (Fig. 4 g). Above achievements demonstrate that the P center in Fe$_2$P phase is primarily responsible to speed up the kinetics of four-step OER process in alkaline medium (Fig. 4 h).

The above achievements demonstrate that the excellent catalytic activity and durability of the CoP@Ni$_2$P – Fe$_2$P heterostructures may result from: (1) The direct growth of 1D hierarchical CoP@Ni$_2$P – Fe$_2$P heterostructure active catalyst on 3D NF substrates effectively avoids the use of binder, while creating stronger guest–host connection/interaction to improve the electroactive surface area, conductivity, and mechanical properties; and (2) the formation of triphasic CoP−Ni$_2$P – Fe$_2$P heterostructure interfaces create abundant defects to expose more active sites. In addition, this also leads to the charge redistribution to optimize the ΔG$_{H*}$ and improve the intrinsic activity towards catalytic reactions.

The excellent electrocatalytic performances of the triphasic CoP@-Ni$_2$P – Fe$_2$P heterostructure catalyst towards both HER and OER encourage us to apply it to the fabrication of a two-electrode electrolyzer cell operating in alkaline medium. In addition, another two-electrode electrolyzer cell of commercial Pt/C$_{(−)}$//RuO$_{2(+)}$ system is also designed for comparison. Fig. 5a shows the LSV response of the CoP@Ni$_2$P – Fe$_2$P$_{(+,−)}$ and Pt/C$_{(−)}$//RuO$_{2(+)}$ devices at a scan rate of 1 mV s^{-1}. It is found that the CoP@Ni$_2$P – Fe$_2$P$_{(+,−)}$ requires only (1.51 or 1.69) V to deliver current densities of (10 or 100) mA cm^{-2}, significantly smaller than that of the Pt/C$_{(−)}$//RuO$_{2(+)}$ of (1.53 or 1.83) V, respectively. The durability of the CoP@Ni$_2$P – Fe$_2$P$_{(+,−)}$ and Pt/C$_{(−)}$//RuO$_{2(+)}$ devices was evaluated by chronoamperometric measurement at an initial current output of 100 mA cm^{-2}. Fig. 5b shows that the activity of CoP@Ni$_2$P – Fe$_2$P$_{(+,−)}$ cell decreases only 3.5 % after continuously running for 40 h, whereas the Pt/C$_{(−)}$//RuO$_{2(+)}$ cell exhibits a significant activity decrease of 17.7 % after only 20 h. The stability of CoP@Ni$_2$P – Fe$_2$P$_{(+,−)}$ cell was also tested at a high current density of 500 mA cm^{-2} during 100 h continuous operation.

Fig. 5c shows that the cell still retains good stable performance with no significant potential fluctuation (3.2 % loss). LSV curves of the CoP@Ni$_2$P – Fe$_2$P$_{(+,−)}$ cell before and after the stability test exhibit good overlapping behavior with the η increase of 19 mV (Fig. 5d), demonstrating such device is stable for long-term operation towards water splitting in alkaline medium. In another regard, the CoP@Ni$_2$P – Fe$_2$P$_{(+,−)}$ further excitingly proves its superior stability for water splitting as compared to early reported catalysts at current density of 100 or 500 mA cm^{-2}, as shown in Table S5, revealing the high potential of CoP@Ni$_2$P – Fe$_2$P for practical water splitting. We constructed a solar energy-driven overall water splitting system by connecting the CoP@Ni$_2$P – Fe$_2$P$_{(+,−)}$ cell with a commercial solar cell to realize the perfect process of green renewable H$_2$ production (Fig. 5e and f). The electrolyzer cell can efficiently perform the water splitting process to produce abundant H$_2$ and O$_2$ gas evolving at cathode and anode, respectively, by using an electric current provided from the solar cell working under AM 1.5 G simulated sunlight irradiation (Fig. 5 g), whereas no bubbles are observed on the electrode surface with the light off (Fig. 5 h). The current density at the intersection between the J−V curve of the solar cell and the LSV curve of the CoP@Ni$_2$P – Fe$_2$P$_{(+,−)}$

electrolyzer cell is found to be 12.46 mA cm^{-2} under simulated solar illumination, consistent with a high STH efficiency value of 15.33 % (Fig. 5i). In addition, the durability of the solar driven overall water splitting system was evaluated by recording the current density responding to light on/off signal. Fig. 5j shows the fast current responses towards many cycles of light on/off. The system could stably work without significant change of current output during 20 h testing under the presence of simulated sunlight irradiation (Fig. 5k), revealing the excellent durability and reliability of the solar driven overall water splitting system. Columbic efficiency or Faraday efficiency (ηF) is calculated to estimate the efficiency of the device in the relationship between external energy source and electrocatalytic process. The ηF of CoP@Ni$_2$P – Fe$_2$P$_{(+,−)}$ can be obtained by calculating the ratio of the actual gas production to the theoretical gas production [66]. Fig. 5 l indicates that the measured H$_2$ and O$_2$ gas volumes are well matched to the theoretical values, resulting in ηF of H$_2$ and O$_2$ evolution being about 98.7 % and 97.7 %, respectively. Since it is compared with previous study, the solar energy-driven overall water splitting system also exhibits superior cell voltage (Fig. 5 m and Table S6) and STH conversion efficiency (Fig. 5 n and Table S7), further evidencing that this system has real potential to produce green hydrogen energy.

4. Conclusions

In this study, we successfully designed novel triphasic CoP−Ni$_2$P – Fe$_2$P heterostructure interfaces appearing under the form of 3D hierarchical core@shell arrays growing on NF substrate. The unique morphology and structure allow the material to possess special physicochemical properties, such as rich multiple electroactive sites, excellent conductivity, and optimum ΔG$_{H*}$, thus demonstrating its role as a powerful bifunctional catalyst toward both HER and OER in alkaline medium. The fabricated CoP@Ni$_2$P – Fe$_2$P$_{(+,−)}$ electrolyzer cell demonstrates a small cell voltage of only 1.51 V at 10 mA cm^{-2}, outperforming the commercial Pt/C$_{(−)}$//RuO$_{2(+)}$ device. The solar driven overall water splitting system also exhibits remarkable performance with a high STH conversion efficiency of 15.33 %, along with good durability for long-term operation. These achievements imply that the CoP@Ni$_2$P – Fe$_2$P may be a promising multifunctional catalyst material to use for the high-efficiency production of green hydrogen energy via solar-assisted electrochemical water splitting.

CRediT authorship contribution statement

Kai Chang: Methodology, Experiment investigation, validation, formal analysis, and writing - original draft. **Duy Thanh Tran**: Conceptualization, writing - reviewing and editing, supervision. **Jingqiang Wang**: Experiment investigation, validation, formal analysis. **Kaixuan Dong**: Experiment investigation and explanation. **Sampath Prabhakaran**: DFT investigation, DFT writing - reviewing and explanation. **Do Hwan Kim**: DFT investigation, DFT writing - reviewing and explanation. **Nam Hoon Kim**: Visualization, writing - reviewing and editing, supervision. **Joong Hee Lee**: Conceptualization, writing - reviewing and editing, supervision.

Declaration of Competing Interest

The authors declare that they have no known competing financial interests or personal relationships that could have appeared to influence the work reported in this paper.

Data availability

Data will be made available on request.

Acknowledgements

Appendix A. Supporting information

Supplementary data associated with this article can be found in the online version at doi:10.1016/j.apcatb.2023.123016.

References

[1] D. Shindell, C.J. Smith, Climate and air-quality benefits of a realistic phase-out of fossil fuels, Nature 573 (2019) 408–411, https://doi.org/10.1038/s41586-019-1554-z.

[2] T.H. Nguyen, P.K.L. Tran, V.A. Dinh, D.T. Tran, N.H. Kim, J.H. Lee, Metal single-site molecular complex–Mxene heteroelectrocatalysts interspersed graphene nanonetwork for efficient dual-task of water splitting and metal–air batteries, Adv. Funct. Mater. (2022), 2210101, https://doi.org/10.1002/adfm.202210101.

[3] J. Ekspong, C. Larsen, J. Stenberg, W.L. Kwong, J. Wang, J. Zhang, E.M. J. Johansson, J. Messinger, L. Edman, T. Wågberg, Solar-driven water splitting at 13.8% solar-to-hydrogen efficiency by an earth-abundant electrolyzer, ACS Sustain. Chem. Eng. 9 (2021) 14070–14078, https://doi.org/10.1021/acssuschemeng.1c03565.

[4] S. Dresp, F. Dionigi, M. Klingenhof, P. Strasser, Direct electrolytic splitting of seawater: opportunities and challenges, ACS Energy Lett. 4 (2019) 933–942, https://doi.org/10.1021/acsenergylett.9b00220.

[5] Y.Q. Zhao, B. Jin, Y. Zheng, H.Y. Jin, Y. Jiao, S.Z. Qiao, Charge state manipulation of cobalt selenide catalyst for overall seawater electrolysis, Adv. Energy Mater. 8 (2018), 1801926, https://doi.org/10.1002/aenm.201801926.

[6] Y. Wang, B. Kong, D.Y. Zhao, H.T. Wang, C. Selomulya, Strategies for developing transition metal phosphides as heterogeneous electrocatalysts for water splitting, Nano Today 15 (2017) 26–55, https://doi.org/10.1016/j.nantod.2017.06.006.

[7] H. Zhang, A.W. Maijenburg, X. Li, S.L. Schweizer, R.B. Wehrspohn, Bifunctional heterostructured transition metal phosphides for efficient electrochemical water splitting, Adv. Funct. Mater. 30 (2020), 2003261, https://doi.org/10.1002/adfm.202003261.

[8] Y. Kuang, M.J. Kenney, Y. Meng, W.H. Hung, Y. Liu, J.E. Huang, R. Prasanna, P. Li, Y. Li, L. Wang, M.C. Lin, M.D. McGehee, X. Sun, H. Dai, Solar-driven, highly sustained splitting of seawater into hydrogen and oxygen fuels, Proc. Natl. Acad. Sci. USA, 116 (2019) 6624–6629. https://doi.org/10.1073/pnas.1900556116.

[9] A. Li, L. Zhang, F. Wang, L. Zhang, L. Li, H. Chen, Z. Wei, Rational design of porous Ni-Co-Fe ternary metal phosphides nanobricks as bifunctional electrocatalysts for efficient overall water splitting, Appl. Catral. B Environ. 310 (2022) 121353, https://doi.org/10.1016/j.apcatb.2022.121353.

[10] L. Chai, S. Liu, S. Pei, C. Wang, Electrodeposited amorphous cobalt-nickel-phosphide-derived films as catalysts for electrochemical overall water splitting, Chem. Eng. J. 420 (2021), 129686, https://doi.org/10.1016/j.cej.2021.129686.

[11] H. Feng, L. Tang, G. Zeng, J. Yu, Y. Deng, Y. Zhou, J. Wang, C. Feng, T. Luo, B. Shao, Nano Energy 67 (2020), 104174, https://doi.org/10.1016/j.nanoen.2019.104174.

[12] H. Huang, A. Cho, S. Kim, H. Jun, A. Lee, J.W. Han, J. Lee, Structural design of amorphous CoMoPx with abundant active sites and synergistic catalysis effect for effective water splitting, Adv. Funct. Mater. 30 (2020), 2003889, https://doi.org/10.1002/adfm.202003889.

[13] Q.L. Han, Y.H. Luo, J.D. Li, X.H. Du, S.J. Sun, Y.J. Wang, G.H. Liu, Z.W. Chen, Efficient NiFe-based oxygen evolution electrocatalysts and origin of their distinct activity, Appl. Catal. B Environ. 304 (2022) 120937, https://doi.org/10.1016/j.apcatb.2021.120937.

[14] K.T.N. Le, V. Hoa, H.T. Le, D.T. Tran, N.H. Kim, J.H. Lee, Multi-interfacial engineering of IrOx clusters coupled porous zinc phosphide-zinc phosphate heterostructure for efficient water splitting, Appl. Surf. Sci. 600 (2022) 154206, https://doi.org/10.1016/j.apsusc.2022.154206.

[15] X. Zhang, J. Li, Y. Yang, S. Zhang, H. Zhu, X. Zhu, H. Xing, Y. Zhang, B. Huang, S. Guo, E. Wang, Co3O4/Fe0.33Co0.66P interface nanowire for enhancing water oxidation catalysis at high current density, Adv. Mater. 30 (2018), 1803551, https://doi.org/10.1002/adma.201803551.

[16] Y. Luo, L. Tang, U. Khan, Q. Yu, H.M. Cheng, X. Zou, B. Liu, Morphology and surface chemistry engineering toward pH-universal catalysts for hydrogen evolution at high current density, Nat. Commun. 10 (2019) 269, https://doi.org/10.1038/s41467-018-07792-9.

[17] G.Q. Zhao, K. Rui, S.X. Dou, W.P. Sun, Heterostructures for electrochemical hydrogen evolution reaction: a review, Adv. Funct. Mater. 28 (2018), 1803291, https://doi.org/10.1002/adfm.201803291.

[18] W. Yuan, T. Jiang, X. Fang, Y. Fan, S. Qian, Y. Gao, N. Cheng, H. Xue, J. Tian, Interface engineering of S-doped Co2P@Ni2P core-shell heterostructures for efficient and energy-saving water splitting, Chem. Eng. J. 439 (2022), 135743, https://doi.org/10.1016/j.cej.2022.135743.

[19] L. Wu, L. Yu, F. Zhang, B. McElhenny, D. Luo, A. Karim, S. Chen, Z. Ren, Heterogeneous bimetallic phosphide Ni2P-Fe2P as an efficient bifunctional catalyst for water/seawater splitting, Adv. Funct. Mater. 31 (2021), 2006484 ttps://doi.org/10.1002/adfm.202006484.

[20] D. Li, C. Zhou, R. Yang, Y. Xing, S. Xu, D. Jiang, D. Tian, W. Shi, Interfacial engineering of the CoxP–Fe2P heterostructure for efficient and robust electrochemical overall water splitting, ACS Sustain. Chem. Eng. 9 (2021) 7737–7748, ttps://doi.org/10.1021/acssuschemeng.0c09377.

[21] H. Liu, J. Gao, X. Xu, Q. Jia, L. Yang, S. Wang, D. Cao, Oriented construction Cu3P and Ni2P heterojunction to boost overall water splitting, Chem. Eng. J. 448 (2022), 137706, https://doi.org/10.1016/j.cej.2022.137706.

[22] S.-H. Cai, X.-N. Chen, M.-J. Huang, J.-Y. Han, Y.-W. Zhou, J.-S. Li, Interfacial engineering of nickel/iron/ruthenium phosphides for efficient overall water splitting powered by solar energy, J. Mater. Chem. A 10 (2022) 772–778, https://doi.org/10.1039/D1TA08385F.

[23] H. Xu, J. Zhu, P. Wang, D. Chen, C. Zhang, M. Xiao, Q. Ma, H. Bai, R. Qin, J. Ma, S. Mu, Fe–Co–P multi-heterostructure arrays for efficient electrocatalytic water splitting, J. Mater. Chem. A 9 (2021) 24677–24685, https://doi.org/10.1039/D1TA06603J.

[24] K. Chang, D.T. Tran, J.Q. Wang, S. Prabhakaran, D. Kim, N.H. Kim, J.H. Lee, Atomic heterointerface engineering of Ni2P-NiSe2 nanosheets coupled ZnP-based arrays for high-efficiency solar-assisted water splitting, Adv. Funct. Mater. 32 (2022), 2113224, https://doi.org/10.1002/adfm.202113224.

[25] P.K.L. Tran, M.S. Kim, T.H. Nguyen, D.T. Tran, N.H. Kim, J.H. Lee, Interfacial engineering for design of novel 2D cobalt sulfide-Mxene heterostructured catalyst toward alkaline water splitting, Funct. Compos. Struct. 3 (2021), 045005, https://doi.org/10.1088/2631-6331/ac3ddc.

[26] M.R. Kandel, U.N. Pan, P.P. Dhakal, R.B. Ghising, T.T. Nguyen, J. Zhao, N.H. Kim, J.H. Lee, Unique heterointerface engineering of Ni2P−MnP nanosheets coupled Co2P nanoflowers as hierarchical dual-functional electrocatalyst for highly proficient overall water-splitting, Appl. Catal. B Environ. 331 (2023), 122680, https://doi.org/10.1016/j.apcatb.2023.122680.

[27] T.-W. Wang, T.-L. Wang, W.-J. Chou, L.-F. Wua, S.-H. Lin, First-principles investigation of the hydrogen evolution reaction of transition metal phosphides CrP, MnP, FeP, CoP, and NiP, Phys. Chem. Chem. Phys. 23 (2021) 2305–2312, https://doi.org/10.1039/D0CP04789A.

[28] T.L.L. Doan, D.T. Tran, D.C. Nguyen, D.H. Kim, N.H. Kim, J.H. Lee, Rational engineering CoxOy nanosheets via phosphorous and sulfur dual-coupling for enhancing water splitting and Zn–air battery, Adv. Funct. Mater. 31 (2020), 2007822, https://doi.org/10.1002/adfm.202007822.

[29] M. Wan, Z. Wan, X.Y. Meng, Z.H. Li, X.G. Ding, P. Li, C. Li, J.G. Wang, Z. Li, Heterostructured Co/Mo-sulfide catalyst enables unbiased solar water splitting by integration with perovskite solar cells, Appl. Catal. B Environ. 309 (2022), 121272, https://doi.org/10.1016/j.apcatb.2022.121272.

[30] C. Lyu, J. Cheng, K. Wu, J. Wu, N. Wang, Z. Guo, P. Hu, W.-M. Lau, J. Zheng, Interfacial electronic structure modulation of CoP nanowires with FeP nanosheets for enhanced hydrogen evolution under alkaline water/seawater electrolytes, Appl. Catal. B Environ. 317 (2022), 121799, https://doi.org/10.1016/j.apcatb.2022.121799.

[31] J. Li, G. Zheng, One-dimensional earth-abundant nanomaterials for water-splitting electrocatalysts, Adv. Sci. 4 (2017), 1600380, https://doi.org/10.1002/advs.201600380.

[32] H.C. Sun, J.M. Yang, J.G. Li, Z.S. Li, X. Ao, Y.Z. Liu, Y. Zhang, Y. Li, C.D. Wang, J. Tang, Synergistic coupling of NiTe nanoarrays with RuO2 and NiFe-LDH layers for high-efficiency electrochemical-/photovoltage-driven overall water splitting, Appl. Catal. B Environ. 272 (2020), 118988, https://doi.org/10.1016/j.apcatb.2020.118988.

[33] H. Wang, H. Zou, Y. Liu, Z. Liu, W. Sun, K.A. Lin, T. Li, S. Luo, Ni2P nanocrystals embedded Ni-MOF nanosheets supported on nickel foam as bifunctional electrocatalyst for urea electrolysis, Sci. Rep. 11 (2021) 21414, https://doi.org/10.1038/s41598-021-00776-8.

[34] F.Y. Tian, D. Hou, W.M. Zhang, X.Q. Qiao, D.S. Li, Synthesis of a Ni2P/Ni12P5 bi-phase nanocomposite for the efficient catalytic reduction of 4-nitrophenol based on the unique n-n heterojunction effects, Dalton Trans. 46 (2017) 14107–14113, https://doi.org/10.1039/c7dt02375h.

[35] J. Yang, Y. Ouyang, H.J. Zhang, H.T. Xu, Y. Zhang, Y. Wang, Novel Fe2P/graphitized carbon yolk/shell octahedra for high-efficiency hydrogen production and lithium storage, J. Mater. Chem. A 4 (2016) 9923–9930, https://doi.org/10.1039/c6ta03501a.

[36] S.J. Patil, N.R. Chodankar, S.-K. Hwang, P.A. Shinde, G. Seeta Rama Raju, K. Shanmugam Ranjith, Y.S. Huh, Y.-K. Han, Co-metal-organic framework derived CoSe2@MoSe2 core-shell structure on carbon cloth as an efficient bifunctional catalyst for overall water splitting, Chem. Eng. J. 429 (2022) 132379, https://doi.org/10.1016/j.cej.2021.132379.

[37] K.J. Zhu, J. Liu, S.T. Li, L.L. Liu, L.Y. Yang, S.L. Liu, H. Wang, T. Xie, Ultrafine cobalt phosphide nanoparticles embedded in nitrogen-doped carbon matrix as a superior anode material for lithium ion batteries, Adv. Mater. Interfaces 4 (2017), 1700377, https://doi.org/10.1002/admi.201700377.

[38] H. Yan, Y. Xie, A. Wu, Z. Cai, L. Wang, C. Tian, X. Zhang, H. Fu, Anion-modulated HER and OER activities of 3D Ni-V-based interstitial compound heterojunctions for high-efficiency and stable overall water splitting, Adv. Mater. 31 (2019), e1901174, https://doi.org/10.1002/adma.201901174.

[39] L. Feng, X. Zhang, J. Huang, D. He, X. Li, Q. Liu, Y. Feng, G. Li, G. Xu, L. Cao, Fe2P encapsulated in carbon nanowalls decorated with well-dispersed Fe3C nanodots for efficient hydrogen evolution and oxygen reduction reactions, Nanoscale 13 (2021) 17920–17928, https://doi.org/10.1039/d1nr03380h.

[40] D.Y. Liu, Q. Zeng, H. Liu, C.Q. Hu, D. Chen, L. Xu, J. Yang, Combining the core-shell construction with an alloying effect for high efficiency ethanol

electrooxidation, Cell Rep. Phys. Sci. 2 (2021), 100357, https://doi.org/10.1016/j.xcrp.2021.100357.

[41] M.S. Yun, T.H. Nguyen, D.T. Tran, N.H. Kim, J.H. Lee, Ultrasmall molybdenum-iron nitride nanoparticles confined carbon nanotubes hybrids for efficient overall water splitting, Funct. Compos. Struct. 4 (2022), 035008, https://doi.org/10.1088/2631-6331/ac93e4.

[42] J. Wang, D.T. Tran, K. Chang, S. Prabhakaran, D. Kim, N.H. Kim, J.H. Lee, Atomic heterointerface engineering of nickel selenide confined nickel molybdenum nitride for high-performance solar-driven water splitting, Energy Environ. Mater. 0 (2022), e12526, https://doi.org/10.1002/eem2.12526.

[43] J.J. Lv, L.M. Wang, R.S. Li, K.Y. Zhang, D.F. Zhao, Y.Q. Li, X.J. Li, X.B. Huang, G. Wang, Constructing a hetero-interface composed of oxygen vacancy-enriched Co₃O₄ and crystalline-amorphous NiFe-LDH for oxygen evolution reaction, ACS Catal. 11 (2021) 14338–14351, https://doi.org/10.1021/acscatal.1c03960.

[44] R. Yang, X. Zheng, M. Qin, B. Lin, X. Shi, Y. Wang, A trifunctional Ni-P/Fe-P collaborated electrocatalyst enables self-powered energy systems, Adv. Sci. 9 (2022), e2201594, https://doi.org/10.1002/advs.202201594.

[45] J. Gautam, D.T. Tran, T.I. Singh, N.H. Kim, J.H. Lee, Mesoporous iron sulfide nanoparticles anchored graphene sheet as an efficient and durable catalyst for oxygen reduction reaction, J. Power Sources 427 (2019) 91–100, https://doi.org/10.1016/j.jpowsour.2019.04.075.

[46] Y. Gu, C.Q. Meng, S.Y. Dong, H.X. Zhu, Q. Liu, Y.L. Luo, Q.Q. Kong, T.S. Li, Electrodeposition of amorphous Fe-P shell on Co(OH)F nanowire arrays for boosting oxygen evolution electrocatalysis in alkaline media, Chemnanomat 8 (2022), e202200085, https://doi.org/10.1002/cnma.202200085.

[47] Z.C. Wu, X. Wang, J.S. Huang, F. Gao, A Co-doped Ni-Fe mixed oxide mesoporous nanosheet array with low overpotential and high stability towards overall water splitting, J. Mater. Chem. A 6 (2018) 167–178, https://doi.org/10.1039/c7ta07956g.

[48] C.F. Li, J.W. Zhao, L.J. Xie, J.Q. Wu, G.R. Li, Fe doping and oxygen vacancy modulated Fe-Ni₅P₄/NiFeOH nanosheets as bifunctional electrocatalysts for efficient overall water splitting, Appl. Catal. B Environ. 291 (2021) 119987, https://doi.org/10.1016/j.apcatb.2021.119987.

[49] D. Zheng, L.H. Yu, W.X. Liu, X.J. Dai, X.X. Niu, W.Q. Fu, W.H. Shi, F.F. Wu, X. H. Cao, Structural advantages and enhancement strategies of heterostructure water-splitting electrocatalysts, Cell Rep. Phys. Sci. 2 (2021), 100443, https://doi.org/10.1016/j.xcrp.2021.100443.

[50] Y.D. Yu, J. Zhou, Z.M. Sun, Novel 2D transition-metal carbides: ultrahigh performance electrocatalysts for overall water splitting and oxygen reduction, Adv. Funct. Mater. 30 (2020), 2000570, https://doi.org/10.1002/adfm.202000570.

[51] T.Y. Wang, C. Wang, Y. Jin, A. Sviripa, J.S. Liang, J.T. Han, Y.H. Huang, Q. Li, G. Wu, Amorphous Co-Fe-P nanospheres for efficient water oxidation, J. Mater. Chem. A 5 (2017) 25378–25384, https://doi.org/10.1039/c7ta08720a.

[52] H.B. Liu, L. Yang, K.W. Qiao, X.F. Zeng, Y. Huang, L.R. Zheng, D.P. Cao, A new concept analogous to homogeneous catalysis to construct in-situ regenerative electrodes for long-term oxygen evolution reaction, Nano Energy 76 (2020), 105115, https://doi.org/10.1016/j.nanoen.2020.105115.

[53] C. Mahala, M.D. Sharma, M. Basu, Fe-doped nickel hydroxide/nickel oxyhydroxide function as an efficient catalyst for the oxygen evolution reaction, ChemElectroChem 6 (2019) 3488–3498, https://doi.org/10.1002/celc.201900857.

[54] Y.T. Wu, C.Y. Sun, H. Wang, S. Ji, B.G. Pollet, J. Lu, X.L. Tian, H.G. Liang, X. Y. Wang, R.F. Wang, Ni₂P nanoparticles-inserted NiFeP nanosheets with rich interfaces as efficient catalysts for the oxygen evolution reaction, J. Alloy. Compd. 903 (2022), 163855, https://doi.org/10.1016/j.jallcom.2022.163855.

[55] Y. Li, Y.Y. Wu, H.R. Hao, M.K. Yuan, Z. Lv, L.L. Xu, B. Wei, In situ unraveling surface reconstruction of Ni₅P₄@FeP nanosheet array for superior alkaline oxygen evolution reaction, Appl. Catal. B Environ. 305 (2022), 121033, https://doi.org/10.1016/j.apcatb.2021.121033.

[56] A. Dutta, N. Pradhan, Developments of metal phosphides as efficient OER precatalysts, J. Phys. Chem. Lett. 8 (2017) 144–152, https://doi.org/10.1021/acs.jpclett.6b02249.

[57] X. Xu, F. Song, X. Hu, A nickel iron diselenide-derived efficient oxygen-evolution catalyst, Nat. Commun. 7 (2016) 12324, https://doi.org/10.1038/ncomms12324.

[58] R. Fernandes, A. Chunduri, S. Gupta, R. Kadrekar, A. Arya, A. Miotello, N. Patel, Exploring the hydrogen evolution capabilities of earth-abundant ternary metal borides for neutral and alkaline water-splitting, Electrochim. Acta 354 (2020), 136738, https://doi.org/10.1016/j.electacta.2020.136738.

[59] P. Wang, R. Qin, P. Ji, Z. Pu, J. Zhu, C. Lin, Y. Zhao, H. Tang, W. Li, S. Mu, Synergistic coupling of ni nanoparticles with Ni₃C nanosheets for highly efficient overall water splitting, Small 16 (2020), e2001642, https://doi.org/10.1002/smll.202001642.

[60] P.Y. Wang, J.W. Zhu, Z.H. Pu, R. Qin, C.T. Zhang, D. Chen, Q. Liu, D.L. Wu, W. Q. Li, S.L. Liu, J.S. Xiao, S.C. Mu, Interfacial engineering of Co nanoparticles/Co₂C nanowires boosts overall water splitting kinetics, Appl. Catal. B Environ. 296 (2021), 120334, https://doi.org/10.1016/j.apcatb.2021.120334.

[61] S.S. Li, L. Wang, H. Su, A.N. Hong, Y.X. Wang, H.J. Yang, L. Ge, W.Y. Song, J. Liu, T.Y. Ma, X.H. Bu, P.Y. Feng, Electron redistributed S-doped nickel iron phosphides derived from one-step phosphatization of MOFs for significantly boosting electrochemical water splitting, Adv. Funct. Mater. 32 (2022), 2200733, https://doi.org/10.1002/adfm.202200733.

[62] R.F. Tian, S.J. Zhao, J.K. Li, Z.B. Chen, W.F. Peng, Y. He, L.L. Zhang, S. Yan, L. L. Wu, R. Ahuja, H.Y. Gou, Pressure-promoted highly-ordered Fe-doped-Ni₂B for effective oxygen evolution reaction and overall water splitting, J. Mater. Chem. A 9 (2021) 6469–6475, https://doi.org/10.1039/d0ta10010b.

[63] L. Ji, Y. Wei, P. Wu, M. Xu, T. Wang, S. Wang, Q. Liang, T.J. Meyer, Z. Chen, Heterointerface engineering of Ni₂P–Co₂P nanoframes for efficient water splitting, Chem. Mater. 33 (2021) 9165–9173, https://doi.org/10.1021/acs.chemmater.1c02609.

[64] J. Wang, D.T. Tran, K. Chang, S. Prabhakaran, J. Zhao, D.H. Kim, N.H. Kim, J. H. Lee, Hierarchical Ni@CNTs-bridged MoₓC/Ni₂P heterostructure micro-pillars for enhanced seawater splitting and Mg/seawater battery, Nano Energy 111 (2023), 108440, https://doi.org/10.1016/j.nanoen.2023.108440.

[65] X. Luo, P. Ji, P. Wang, R. Cheng, D. Chen, C. Lin, J. Zhang, J. He, Z. Shi, N. Li, S. Xiao, S. Mu, Interface engineering of hierarchical branched Mo-doped Ni₃S₂/NiₓPᵧ hollow heterostructure nanorods for efficient overall water splitting, Adv. Energy Mater. 10 (17) (2020), 1903891, https://doi.org/10.1002/aenm.201903891.

[66] C.L. Xiao, Y.B. Li, X.Y. Lu, C. Zhao, Bifunctional porous NiFe/NiCo₂O₄/ni foam electrodes with triple hierarchy and double synergies for efficient whole cell water splitting, Adv. Funct. Mater. 26 (2016) 3515–3523, https://doi.org/10.1002/adfm.201505302.